communications earth & environment

ARTICLE

https://doi.org/10.1038/s43247-021-00265-w OPEN

Formation of giant iron oxide-copper-gold deposits by superimposed, episodic hydrothermal pulses

Irene Del Real[1,2✉], Martin Reich[1,2], Adam C. Simon[3], Artur Deditius[4], Fernando Barra[1,2], María A. Rodríguez-Mustafa[3], John F. H. Thompson[5] & Malcolm P. Roberts[6]

Iron oxide-copper-gold deposits are a globally important source of copper, gold and critical commodities. However, they possess a range of characteristics related to a variety of tectono-magmatic settings that make development of a general genetic model challenging. Here we investigate micro-textural and compositional variations in actinolite, to constrain the thermal evolution of the Candelaria iron oxide-copper-gold deposit in Chile. We identify at least two mineralization stages comprising an early 675–800 °C iron oxide-apatite type mineralization overprinted by a later copper-rich fluid at around 550–700 °C. We propose that these distinct stages were caused by episodic pulses of injection of magmatic-hydrothermal fluids from crystallizing magmas at depth. We suggest that the mineralisation stages we identify were the result of temperature gradients attributable to changes in the magmatic source, rather than variations in formation depth, and that actinolite chemistry can be used as a proxy for formation temperature in iron oxide-copper-gold systems.

[1] Department of Geology, FCFM, Universidad de Chile, Plaza Ercilla 803, Santiago, Chile. [2] Millennium Nucleus for Metal Tracing Along Subduction, FCFM, Universidad de Chile, Santiago, Chile. [3] Department of Earth and Environmental Sciences, University of Michigan, Ann Arbor, MI, USA. [4] Chemistry and Physics, Murdoch University, Perth, WA 6150, Australia. [5] PetraScience Consultants, 3995 West 24th Avenue, Vancouver, BC V6S 1M1, Canada. [6] Centre for Microscopy, Characterisation and Analysis (CMCA), University of Western Australia, Perth, WA 6009, Australia. ✉email: idelreal@gmail.com

Iron oxide-copper-gold (IOCG) systems are among the world's richest mineral deposits, making for highly profitable mining operations[1–3]. By-product strategic elements including Co, U and REE add to their attractiveness. Previous studies on important IOCG deposits, such as Olympic Dam (Australia), Candelaria (Chile), and Salobo and Sossego (Brazil), have shown that they are closely related to basement penetrating fault systems[1,2], and have undergone an early magnetite-actinolite event followed by main-stage mineralization of copper and other elements[4–6]. Even though there is abundant evidence for magmatic signatures in IOCG deposits—geochemical and isotopic[1,3,7]—most of these deposits show no apparent genetic relationship with exposed coeval igneous intrusions[1–3,7]. Intrusions are inferred at depth but the magmatic events leading to mineralization are not well defined. Geochemical proxies, particularly the chemical composition and Fe-O-H-S isotopic signatures of selected silicates, magnetite, and pyrite, have provided some insights into the nature of the hydrothermal fluids[8–17]. Despite this progress, the thermal evolution of IOCG systems in space and time remains poorly constrained as IOCG deposits lack substantial quartz veining hindering the use of fluid inclusion data[18–22]. In particular, the thermal and spatial evolution constraints of early Cu-poor and Fe-rich alteration and the main Cu(-Au) mineralization stages have not been addressed. Understanding the temporal and spatial relationship between these two stages is critical to development of a universally applicable genetic model. One of the most common minerals found in both (early) Fe-rich and (later) Cu-rich mineralization stages in IOCG deposits is actinolite, $(Ca_2)(Mg_{4.5-2.2}Fe_{0.5-2.5})(Si_8O_{22})(OH)_2$. Experimental data demonstrate that the thermal stability of actinolite depends on its Fe and Mg content, which decrease linearly over a wide P-T range, and is applicable as a proxy for estimating temperature of formation[23]. Compositional variations in minerals have been used previously for temperature estimations, e.g., titanium content in zircons[24] or Mg-Fe silicate minerals in porphyry Cu-Au-Mo systems[25–31]. In the case of actinolite, its composition has been successfully used for estimating temperature of formation in IOA and Cu-Ni-PGE deposits[16,23,32–34], and preliminary data using actinolite in IOCG deposits suggests that it could be similarly useful[16,35].

In this contribution, we examine micro-textural and compositional variations of actinolite recovered along a ~1 km-long drill core to determine the thermal evolution of the Candelaria IOCG deposit. This study provides the empirical evidence indicating a key role for successive magmatic fluid injections in the formation of IOCG deposits and provides insight on how iron oxide-apatite (IOA) and IOCG deposits genetically relate.

Geology and mineralization in the Candelaria-Punta del Cobre district. The Candelaria-Punta del Cobre district is located south of the city of Copiapó in northern Chile and comprises more than nine active IOCG mines, all interpreted to be part of the same hydrothermal system[6] (Fig. SM1, Supplemental Material). IOCG deposits in this district are spatially and temporally associated with a north-northwest sinistral fault system and are interpreted to be coeval with a northwest transpressive deformation[6]. Copper mineralization is predominantly hosted in the Lower Cretaceous (~135–132 Ma) volcanic-sedimentary Punta del Cobre Formation that is overlain by sedimentary marine sequences from the Lower Cretaceous (132–130 Ma) Chañarcillo Group[6,36]. An early calcic-sodic alteration is observed towards the northwestern side of the district followed by a widespread magnetite-actinolite alteration formed between ~120 and 116 Ma[6]. This early magnetite-rich alteration extends beyond all deposits in the district (both in depth and laterally) and is observed as a fine grained pervasive alteration that can completely replace the volcanic host rocks, sharing similarities with the alteration mineralogy described in IOA deposits[37].

In the Candelaria deposit, Cu-Fe mineralization and its related hydrothermal alteration are hosted mainly in volcanic/volcaniclastic rocks of the Punta del Cobre Formation and extends to depths in excess of 800 m. At these depths the early stage magnetite-actinolite and calcic-sodic alteration assemblages are overprinted by a chalcopyrite-magnetite-biotite–K-feldspar ± pyrite ± actinolite mineralization/alteration dated at ca. 115 Ma that represents the main Cu mineralization stage in the area[6,18]. The main ore body in the Candelaria deposit reaches up to 400 m in thickness in the central part and thins towards the margins[6,18]. Actinolite in the deposit occurs in veins together with Cu-(Fe) sulfides, as massive granular aggregates with magnetite or Cu-(Fe) sulfides, and as fine disseminations in the volcanic host rocks. In all its forms, actinolite is a common alteration mineral in the Candelaria deposit[6] that can be associated with the Cu mineralization stage (Fig. 1a–c) as well as the early Fe stage (Fig. 1a), indicating that the mineral was formed during both alteration/mineralization stages. These two alteration/mineralization stages in the Candelaria district are broadly coeval with the emplacement of the Copiapó Batholith located west of the main deposits[38], but there is no field evidence yet that ore-bearing hydrothermal fluids were sourced directly from the batholith[6].

Actinolite sampling and temperature calculations. Samples for this study were collected from a 1000 m-long drill core that traverses the main Cu ore bodies and the underlying magnetite-rich rocks at Candelaria (Fig. 2). Actinolite was sampled systematically throughout the length of the drill core from both Fe-rich and Cu-rich zones, providing a comprehensive and representative sample set (full description in Table SM1, Supplemental Material). In areas with Cu mineralization, distinguishing petrographically among actinolite from the early Fe and main Cu stages is challenging. However, backscattered electron (BSE) images of the analyzed samples reveal micro-textural variations, including actinolite grains with marked core-to-rim chemical zoning, actinolite overgrowths on earlier actinolite, chemically homogenous actinolite, and small crystal cumulates (Fig. 2; Fig. SM2, Supplemental Material). The different textures identified through BSE images allowed to determine some constraints regarding the different processes involved in the formation of the different actinolite grain types (e.g., overgrowths or replacement), although there is no exact relationship between the textures and each mineralization/alteration stage.

The chemical composition of actinolite was determined using electron probe microanalysis (EPMA; Table SM2, Supplemental Material), including high-resolution quantitative X-ray wavelength-dispersive spectrometry (WDS) maps of representative grains from both stages. Model temperatures were determined using the experimental data of Lledo and Jenkins[23], who derived a polynomial regression based on experimentally controlled crystallization temperatures and the Fe-number ($Fe\# = X_{Fe}/[X_{Fe} + X_{Mg}]$; concentrations are in atomic %) of actinolite for each analysis. The calculated temperature uncertainty for extracting a temperature of stability will depend on the Ca a.p.f.u.[23]. Varying the Ca content from 1.6 to 1.9 a.p.f.u[23] shifts the calculated temperature boundary in about 25 °C for a variation. As our Ca a.p.f.u. results are within this range, our temperature estimation errors are estimated at less than 25 °C.

The composition of actinolite, and therefore its Fe# used for calculating temperatures, can also be sensitive to prograde and retrograde metamorphic reactions[39], amphibole morphology[40],

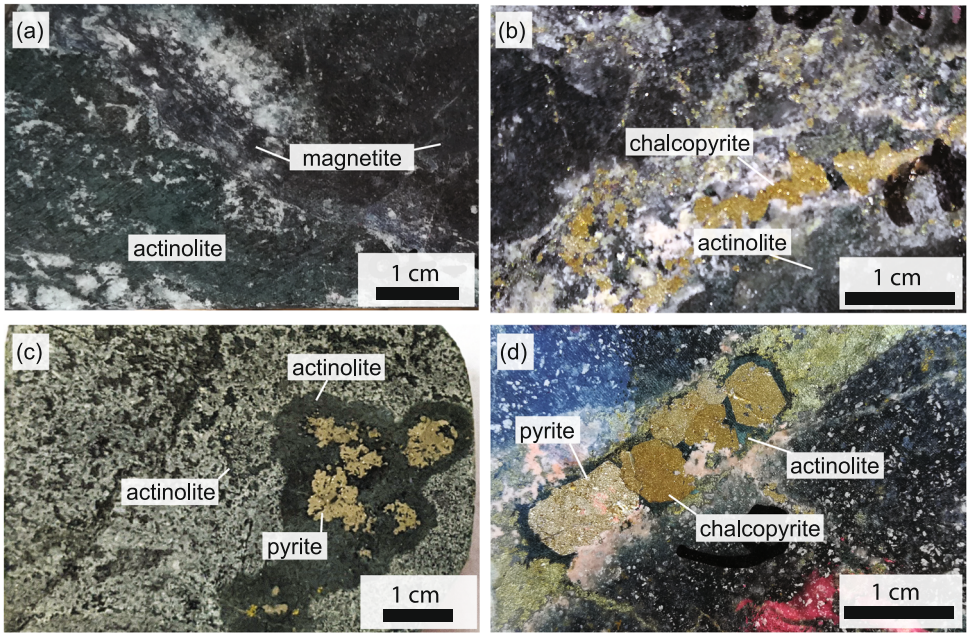

Fig. 1 Drill core samples showing actinolite associated with both the main Cu mineralization and the early Fe stage at the Candelaria deposit. Image (**a**) corresponds to sample LD1687-70 (depth 1109.5 m) where actinolite is observed as a pervasive alteration together with magnetite, but with no Cu sulfides. Image (**b**) corresponds to sample LD1687-35 (depth 585.12 m) where actinolite is observed close to Cu-sulfide mineralization but not clearly coeval. Image (**c**) shows sample LD1687-63 (depth 1001.3 m) where actinolite is observed finely disseminated in the host rock and in a cumulate surrounding pyrite. Image (**d**) shows a chalcopyrite-pyrite-actinolite vein crosscutting the andesite host rock with pervasive actinolite-magnetite alteration (sample LD1687-13 depth 203.6 m). Further details for each sample can be found in Table SM1 (Supplemental Material).

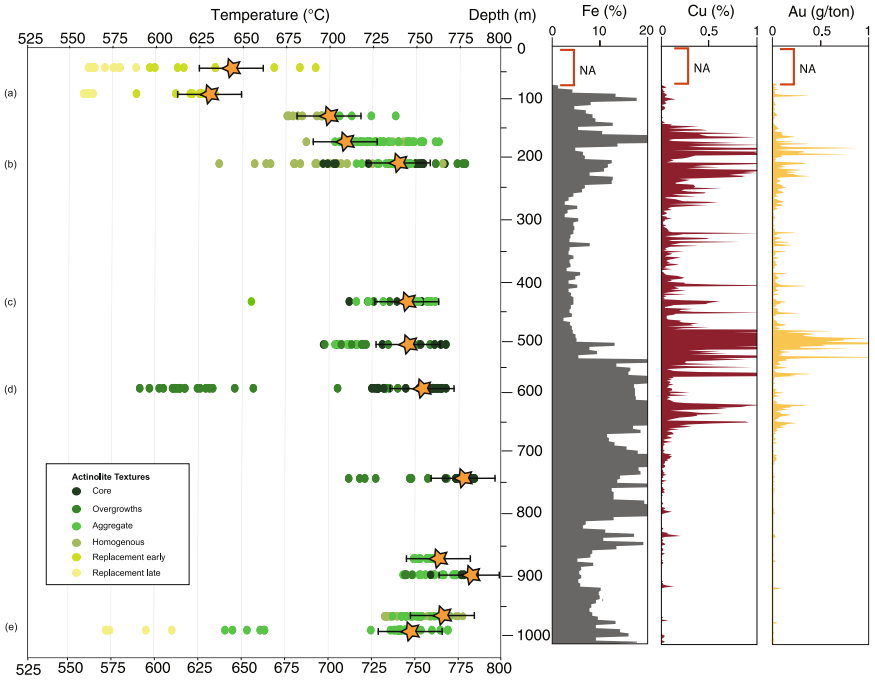

Fig. 2 Calculated temperatures of actinolite crystallization plotted as a function of depth in drill core LD1687. Letters **a**–**e** indicate samples with calculated temperature distribution maps (see Fig. 3). Letters correspond to the maps in Fig. 3. The vertical plots display variation of the Fe, Cu, and Au grades with depth at Candelaria (whole rock data obtained from 2 m-long half drill core samples, Lundin Mining, internal report). Orange stars correspond to average temperature values from early actinolite textures (e.g., grain cores), and error bars correspond to maximum temperature uncertainty when a.p.f.u. Ca deviates from 1.8[23].

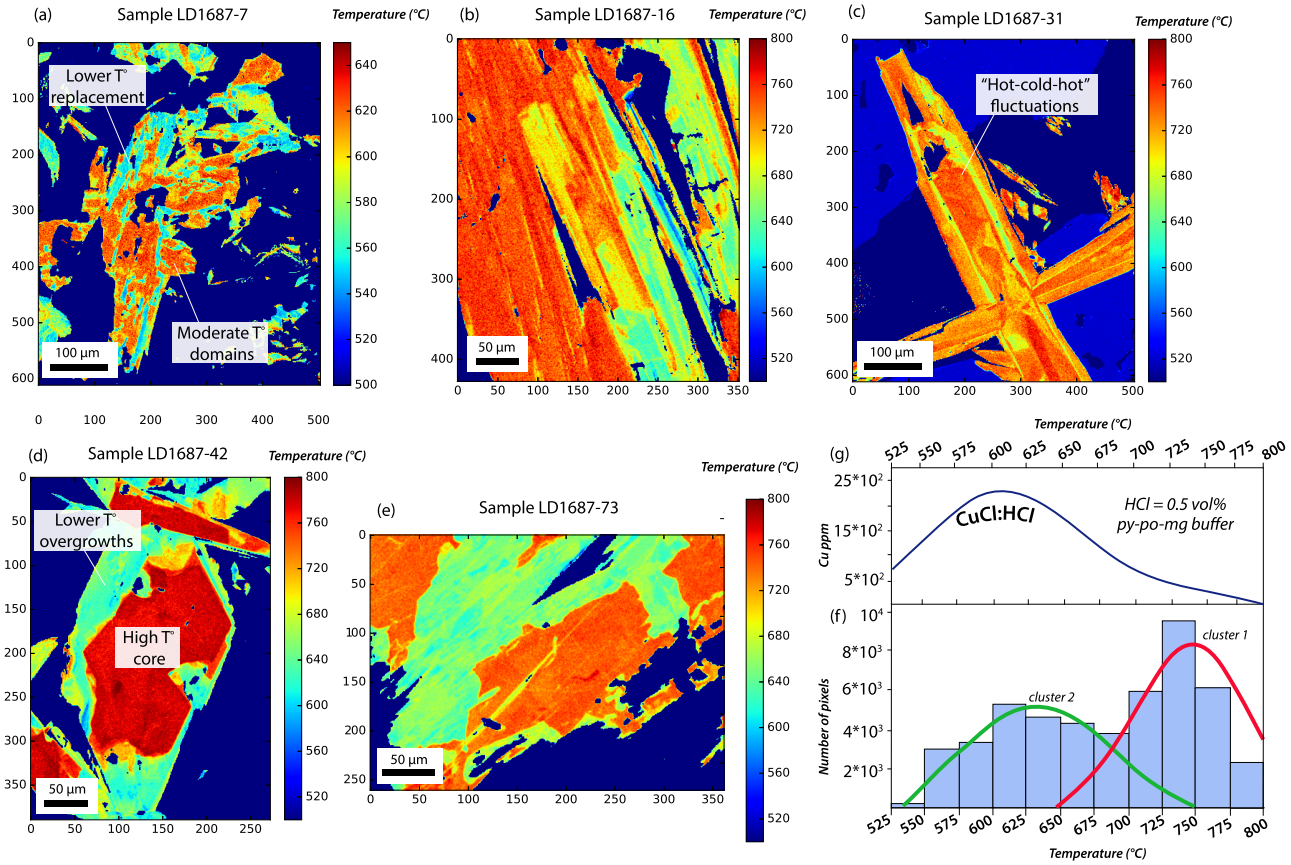

Fig. 3 Temperature variation and zonation of actinolite grains. a–e Grain-scale temperature maps of representative actinolite samples from drill core LD1687. **f** Histogram showing number of pixels extracted from temperature maps vs. actinolite temperatures. **g** Solubility curve of CuCl:HCl as a function of temperature for a HCl-bearing fluid saturated with respect to chalcopyrite; fO_2 conditions correspond to the pyrite-pyrrhotite-magnetite buffer[46]. Temperature maps axis is scaled in micrometers.

large changes in pressure conditions[41], and the presence of coexisting minerals that can incorporate or buffer Fe and Mg[39]. In the Candelaria deposit, the composition of the host rocks is relatively uniform[6], actinolite composition is independent of grain morphology or texture (Fig. 2; Figs. SM2 and SM3), pressure conditions are mostly homogeneous and estimated at about ~1 kbar[16], and there are no important overprinting metamorphic events in the area[6,18]. Although kinetic effects can also influence mineral growth and chemical zoning[42,43], these are not considered to be important in this study as only one sample shows quasi-cyclic zoning (or oscillatory zoning) in its chemical composition (Fig. 3c; Fig. SM3). Therefore we interpret the variation in the composition of actinolite to be predominantly related to changes in temperature. Based on these observations, each EPMA analysis was linked to a corresponding actinolite texture at the microscale, (green circles in Fig. 2; Supplemental Data 1 and Table SM2), and temperatures were calculated for each data point (Supplementary Data 1). Textures, such as core, rim, replacement (early), or replacement (late), were used to establish a temporal relationship of actinolite textures in relation to temperature formation conditions. Temperature averages shown as orange stars in Fig. 2 were determined from the earlier paragenetic textures present in the samples (core or replacement (early)): in samples with no early textures average temperatures were calculated from the remaining textures (cumulate or homogeneous).

In addition to temperatures calculated based on the Fe#, we computationally converted the Fe and Mg concentrations from WDS maps of representative actinolite grains from the Fe- and Cu-rich events into temperature maps. This was achieved by making a volumetric (3D) image stack filled with the WDS maps, which were subsequently reshaped into a planar (2D) array for each element of interest. A polynomial regression based on the Mg-Fe temperature proxy[23] was applied for each pixel using the 2D arrays. This technique allowed visualization of inferred temperature gradients at a microscale within individual actinolite grains, providing insights into temperature fluctuations within and among single crystals (see Methods section).

Results

Calculated actinolite formation temperatures range from ~550 to ~800 °C (Figs. 2 and 3). However, the average temperature calculated for early actinolite grains (i.e., cores and high-temperature overgrowths) increases with depth down the drill hole (orange stars in Fig. 2). The temperatures calculated from the actinolite chemistry show a broadly inverse relationship with Cu and Au grades (Fig. 2).

The maps of temperature distribution in actinolite (Fig. 3) reveal a complex crystallization history, with intracrystalline variations ≥200 °C that reflect strong Fe and Mg zonations (Fig. 3a–e). In the shallow levels of the deposit (row a in Fig. 2), intracrystalline chemical zonation of actinolite reveals domains of moderate temperature (~650–600 °C) surrounded by replacement textures formed at lower temperature (600–550 °C) (Fig. 3a). Overgrowths on actinolite cores with non-equilibrium growth textures are recognized at intermediate to deeper levels of the deposit (Fig. 2, rows b–e), indicating at least two stages of

actinolite formation (Fig. 3b–e). In the deepest levels of the system (Fig. 2, rows d–e), the composition of actinolite cores indicate early high temperatures (~800–750 °C) and overgrowths with lower temperatures (~680–600 °C) (Fig. 3d, e). In some actinolite grains at intermediate depth, alternating compositional layers ("hot-cold-hot") record complex temperature fluctuations that could be interpreted as pulsed crystallization or continuous growth under different kinetic conditions (Fig. 3c).

The intra and intercrystalline grain-scale temperature variations are represented in histograms constructed from each pixel in the temperature maps (Fig. 3f, Fig. SM4 and Supplementary Data 2). Two distinct main temperature clusters are observed in Fig. 3f; a high-temperature cluster-1 (~800–675 °C) and a low-temperature cluster-2 (~700–550 °C). Most actinolite cores display high-temperature values (e.g., Fig. 3d; Table SM2, Supplemental Material) coincident with cluster-1. In contrast, most overgrowths are characterized by lower temperatures concordant with cluster-2 values, and representing a later stage (Table SM2, Supplemental Material). Besides showing distinct differences in their temperature, the two clusters also display differences in their major element compositions, most notably chlorine (Table SM3, Supplemental Material).

Discussion

Temperature controls on mineral precipitation. The two temperature clusters in Fig. 3f indicate that the Candelaria IOCG deposit was formed during two distinct mineralization stages as potentially part of one evolving hydrothermal system. These correspond to a widespread high-temperature magnetite-actinolite stage (cluster-1) and a more localized lower-temperature Cu stage (cluster-2).

The early, high-temperature cluster-1 stage (800–675 °C) is related to abundant magnetite-actinolite that is ubiquitous at depth. At an estimated constant pressure of 100 MPa, Fe(II), which will be transported as $FeCl_2$ in a hydrothermal fluid, will precipitate as magnetite at temperatures above ~500 °C[16,44,45]. These findings indicate that magnetite precipitation, as inferred from calculated actinolite temperatures, occurred over the range 800–550 °C, with most of the data falling within the range of ~800–675 °C (cluster-1; Fig. 3f). The data indicate the presence of a high-temperature Fe-rich stage at Candelaria, which correlates with the early magnetite-actinolite alteration (Fig. 1a) that has been documented in the Candelaria district[6].

In contrast, Cu grades increase at intermediate and shallow levels at Candelaria (Fig. 2), broadly correlating with cluster-2 lower temperatures (cluster-2: 550–700 °C). Cluster-2 temperatures (Fig. 3f) overlap with temperatures over which Cu reaches maximum solubility in a HCl-bearing hydrothermal fluid at 100 MPa, saturated with chalcopyrite at oxygen (fO_2) and sulfur (fS_2) fugacities buffered by the assemblage pyrite-pyrrhotite-magnetite[46] (Fig. 3g). These conditions can be extrapolated to those for the formation of the Candelaria deposit[6,16], where the mineral buffering assemblage for fS_2 is the same as the mineral paragenesis identified in the main ore body[6,18]. Our findings suggest that the low-temperature actinolite (cluster-2), often found as overgrowths on higher-temperature actinolite cores (cluster-1, e.g., Fig. 3d; Table SM2, Supplemental Material), records a hydrothermal event where Cu-rich fluids cooled from ~750 °C to temperatures below ~550 °C[47], explaining the observed broad correspondence between high Cu grades and lower actinolite temperatures (Fig. 2). The implication is that Cu precipitated as chalcopyrite once the hydrothermal fluid cooled below ~550 °C, as indicated by available sulfur isotope and limited fluid inclusion data[15,18] and correspondent with chalcopyrite precipitation temperatures calculated experimentally[47].

The two temperature clusters determined from the composition of actinolite are interpreted as two distinct hydrothermal stages and are consistent with data from other IOCG and IOA deposits. Actinolite cluster-1 temperatures (Fig. 3f) correlate well with values calculated for Andean IOAs using $\delta^{18}O$ and δD isotope thermometry (e.g., Fe-rich stages in the Marcona district in Perú and the Quince prospect in Chile)[16,48] and actinolite chemistry (e.g., El Romeral and Los Colorados deposits in Chile)[32,49]. The paragenesis of the early high-temperature stage in the Candelaria-Punta del Cobre district is identical to the mineralization/alteration paragenesis in Andean IOA deposits (magnetite-actinolite e.g., Cerro Negro Norte, El Romeral, Los Colorados, Marcona)[34,50–52]. Therefore, the early alteration stage in Candelaria is analogous to high-temperature Fe-rich mineralization in IOA deposits. In contrast, lower actinolite temperatures (cluster-2) related to the Cu-rich IOCG stage are consistent with experimentally determined chalcopyrite solubility conditions[46,47] (Fig. 3g).

Mineralization episodes triggered by tapping reservoirs of magmatic-hydrothermal fluids. The observations and modeling reported here support an early, high-temperature Fe-rich stage followed by a lower-temperature Cu-rich one, with magnetite and actinolite ubiquitous to both, but chalcopyrite only occurring in the latter. Figure 4 illustrates a genetic model for the formation of the Candelaria deposit, which relates the early Fe-rich stage with the later Cu-rich mineralization, and can be applied to the whole district and potentially other IOCG deposits. The model takes into account the two distinct hydrothermal stages and is consistent with geological observations and empirical data collected for Cordilleran IOCG systems[6,18,50,53–55]. In addition, it integrates recent models of Fe transport proposed for IOA deposits[56–60]. These two styles of mineralization (IOCG and IOA) commonly overlap in time and space, and several studies have proposed a genetic link between them, with magnetite-rich mineralization corresponding to the deeper hotter roots of Cu-rich (IOCG) systems[7,61–66]. Our model further expands this genetic link by proposing that both styles of mineralization formed at Candelaria by superposition within the same (stratigraphic) levels (Fig. 4).

Trace element data for magnetite and pyrite together with $\delta^{37}Cl$ data from the Candelaria system indicate that hydrothermal fluids in the district were sourced from intermediate to mafic silicate magmas[15,16,67], gabbro to diorite in composition, formed in the Upper Jurassic to Lower Cretaceous magmatic arc of northern Chile[68,69]. Dioritic magmas formed under these conditions would be enriched in volatiles together with Fe, Cu, S, and Cl[70,71]. Exsolution of a magmatic-hydrothermal volatile phase from the silicate melt would start during cooling of the parental magma. Volatile exsolution may be triggered by prior magnetite crystallization, as demonstrated experimentally[59,72,73], where exsolving magmatic-hydrothermal fluid bubbles nucleate on magnetite microlites to form a magnetite-fluid suspension that rises through the intrusive body[57,73] scavenging metals, and forming an accumulation of a metal-rich fluid in the upper part of the magma body[57] (Fig. 4a). This zone of Fe-, Cu-, and S-rich fluid accumulation, analogous to volatile concentration reported for pre-eruptive magma chambers beneath arc volcanoes and processes invoked in the formation of porphyry Cu deposits[74], would go through periodic sealing and rupture potentially related to movement of deep crustal, sinistral strike-slip faults (Fig. 4b). Mineralization in the Candelaria district is hosted in rocks that are ca. 15 Ma older than the main Cu event[6]; therefore, the formation of structurally-related "paths" for hydrothermal fluids to ascend, i.e., the deep crustal sinistral strike-slip faults, would

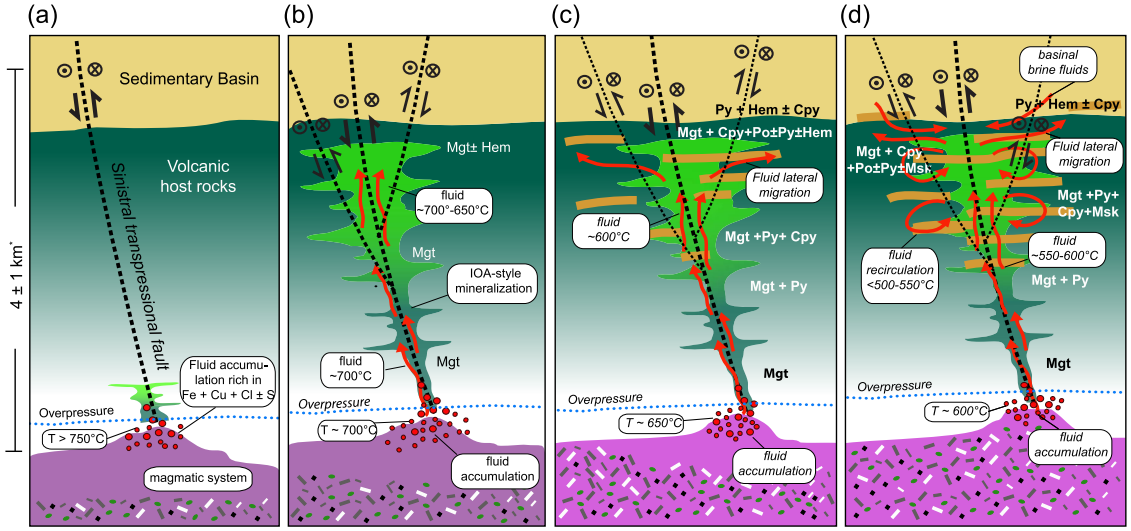

Fig. 4 Schematic model for the Candelaria IOCG district. a Slow cooling of a dioritic intrusion and separation of a fluid phase, coalescence of the fluid phase, and encapsulation of magnetite microlites to form a magnetite-fluid suspension accumulation under overpressure conditions that scavenges Fe, Cu, Au, S, and Cl[57, 58]. **b** The accumulated fluid is sporadically "tapped" by active, deep crustal sinistral strike-slip faults initially associated with the formation of the sedimentary basin. Fault movement allowed the ascent of high-temperature Fe-rich fluids. **c** Further fault movement would allow the ascent of (Cu, Fe)-rich fluids; Cu in the fluid increases due to increased solubility of CuCl at ~650 °C. **d** Fluids cooling to temperatures of about 600 °C; further cooling to ~500 °C of the ascending hydrothermal fluids by convection causes Cu precipitation. Peak chalcopyrite mineralization occurs at temperatures of ~400 °C. At the final stage, hydrothermal fluids would have interacted with external, basin derived fluids, which would have added reduced sulfur into the system in the form of pyrite but no important Cu mineralization[20]. *Depth estimated for pressure conditions of 100 MPa.

have been crucial for fluid flow into older volcano-sedimentary stratigraphy. In the Candelaria-Punta del Cobre district, extensional faults, initiated during the formation of the sedimentary basin that overlays the ore bodies, were inverted at the same time as hydrothermal activity[6]. Increased fault slip would rupture the carapace above crystallizing intrusions and enhance structural permeability in overlying rocks. Fluid flow would be focused by buoyancy-driven propagation through fluid-filled fractures[75], promoting efficient ascent of the deep fluid accumulated in fractures in the upper crystallizing parts of the viscous magma, and allowing fluid redistribution in the shallow levels of the system[76–78] (Fig. 4c). Actively deforming structures can produce pipe-like pathways linking deep reservoirs to shallow crustal levels[79,80]. The process could lead to a repetitive cycle with hydrothermal fault sealing, fluid reaccumulation, increased pressure and consequent fault rupture[81,82]. This "tapping" of the fluid reservoir would permit high-temperature magmatic-hydrothermal fluids to ascend under adiabatic conditions, precipitating early magnetite[44] (Fig. 4b) with paragenetically-related, high-temperature actinolite (cluster-1, Fig. 3g), and generating the Fe-rich, IOA-style of mineralization.

Subsequent evolution of distinct pulse(s) of Cu- and S-bearing magmatic-hydrothermal fluid from the source magmatic system (Fig. 4c) and cooling of this fluid as it ascends through pre-existing superjacent structures results in precipitation of lower-temperature actinolite (cluster-2, Fig. 3g), magnetite (Fe is still soluble at these temperatures), and Cu-(Fe) sulfides (chalcopyrite and pyrite, once the fluid cools to temperatures lower than ~550 °C). If the hydrothermal fluid is oxidized[15,16], it would precipitate hematite instead of magnetite, consistent with observations in some IOCG deposits, such as Mantoverde[22,53] (Chile) and Olympic Dam[83,84] (Australia). Repeated, temporally distinct, fault reactivation may result in different pulses of hydrothermal activity as evidenced by actinolite micro-textures (Fig. 3a–e) and by overlapped actinolite and sulfide mineralization (Fig.1d). Further, if the fluid reservoir is periodically recharged with fluids from the underlying magmatic system, compositionally banded textures observed in actinolite grains would record such temperature (and fluid composition) fluctuations (Fig. 3c).

The main Cu mineralization stage at Candelaria would have occurred when ascending fluid(s) cooled to temperatures below ~550 °C precipitating chalcopyrite, due to the sharp drop in chalcopyrite solubility[47] (Fig. 3g; Fig. 4d). Furthermore, the presence of early magnetite might have facilitated the precipitation of Cu sulfides[85], as suggested by geological observations and petrographic evidence of chalcopyrite replacing early magnetite in the Candelaria deposit (Fig. SM5). As cooling progresses, chalcopyrite precipitation will continue, reaching a peak at temperatures of 550–400 °C[15,18,47] (Fig. 4d).

The observation of two temporally distinct hydrothermal alteration/mineralization stages is consistent with episodic replenishment of an evolving crustal magmatic system where the magmatic-hydrothermal fluid evolve from newly emplaced magma that either underplates previously emplaced magma or forcibly intrudes and mixes with previously emplaced magma[76,77]. Such buoyancy-driven outgassing of magmatic-hydrothermal fluid from magma can efficiently transfer fluid-soluble elements such as those found in IOCG deposits[76]. The chemistry of a magmatic-hydrothermal fluid exsolved from a silicate melt is controlled by the pressure, temperature, oxidation state, and composition of the melt from which it exsolves[86,87]. The low concentration of Cu and S in the first fluid stage, evidenced by the modally minor amount of sulfide coeval with early magnetite and actinolite, is consistent with the evolution of a magmatic-hydrothermal fluid from a magma that had lost Cu and S to a sulfide crystal/liquid, which was not subsequently resorbed prior to degassing and was not resorbed during the degassing event[86,88]. The fluid responsible for the subsequent Cu-sulfide-rich stage could have outgassed from the same evolving

magma body and resulted in resorption of earlier formed Cu-sulfide crystal/liquid, or could have evolved from a newly emplaced magma where the released volatiles overcame capillary resistance and ascended along permeable channels developed in overlying, older crystal mush[77]. The efficient ascent of a magmatic-hydrothermal fluid in such evolving magmatic systems is transient and dependent entirely on the rate of supply of ascending magmatic-hydrothermal fluid[78]. Intermittent degassing events could explain the superimposed magnetite-actinolite and younger magnetite-actinolite-Cu-sulfide mineralization events at Candelaria. The precise timing between hydrothermal stages is yet to be properly evaluated by further geochronological studies. Understanding the timeframe between these two stages in the Candelaria-Punta del Cobre district will be essential for better characterizing the magmatic evolution of the hydrothermal system responsible for mineralization, and its connection to magmatic sources.

A different paradigm that connects IOA and IOCG mineralization. Our genetic model involving at least two distinct stages of hydrothermal activity introduces an important addition to how we understand the evolution and connection between IOA and IOCG mineralization styles. As noted, previous studies have suggested a spatial and temporal relationship between IOA and IOCG mineralization, where the IOA could represent the roots of an IOCG system[7,58,62,64]. Further, the presence of minor sulfides in IOA deposits (e.g., Los Colorados, El Romeral, Cerro Negro Norte)[52] and early, pre-Cu mineralization, magnetite-actinolite in IOCG deposits (e.g., El Espino, Mantoverde, Mina Justa, Raúl Condestable, Dominga)[50,53–55,89] point to a transition between IOA and shallow IOCG mineralization styles. However, those authors assumed that both IOA and IOCG mineralization were the result of a single cooling fluid. Although this may be the case for IOA deposits and small, vein-type IOCG systems[7,58,62,64], our data reveal that there were at least two distinct stages of hydrothermal activity involved in the formation of a world-class IOCG deposit, which are superimposed. These stages correspond to hydrothermal fluids of contrasting temperatures, and possibly with distinct ligand and metal budgets derived from an evolving magmatic source(s).

Conclusions

The deposit-scale actinolite data presented here are used as a proxy to determine mineralization temperatures and provide a tool to trace the evolution of IOCG mineral systems. Furthermore, our results offer a different explanation for how the Cu-deficient IOA-type mineralization relates spatially to Cu-rich IOCG deposits. We propose that both mineralization styles can represent temporally distinct nonequivalent hydrothermal stages albeit part of the same metallogenic system. We argue that IOA-type and IOCG mineralization styles should not necessarily be viewed as related to formation depth, but rather be the result of temperature gradients and an evolving magmatic source affecting hydrothermal fluid composition and circulation. Most importantly, we argue that world-class IOCG deposits such as Candelaria are formed by distinct, episodic pulses of hydrothermal activity. The detailed understanding of the characteristics and key controls of the magmatic-hydrothermal evolution responsible for the formation of large IOCG deposits, and therefore the factors that control metal transfer, is a critical step in the development of new strategies for successful exploration. Therefore, the results presented here open opportunities for Cu exploration in districts that are historically rich in Fe. It also supports the use of compositional variations in actinolite as a proxy for formation temperature estimates that could potentially be applied to determine thermal gradients at the district and even regional scales, and hence could be used as an effective vectoring tool.

Methods

Electron microprobe point analysis was performed at the Electron Microbeam Analysis Laboratory, University of Michigan by using a Cameca SX-100 with a voltage of 15 kV, a current of 20 nA and a 2 μm beam. We measured Si, Ti, Al, V, Cr, Mn, Fe, Ni, Mg, Ca, Na, F, and Cl. All results, counting times, standards, and detection limits are listed in the Supplemental Material.

WDS X-ray maps were acquired on a JEOL 8530 F field-emission electron probe microanalyzer equipped with five wavelength-dispersive spectrometers at the Center for Microscopy, Characterization and Analysis (CMCA), University of Western Australia, Perth, WA. The elements Si, Ti, Al, Mn, Fe, Mg, Ca, Na, and Cl were measured. Detection limit maps were acquired for these elements and applied as the minimum cutoff values. Map acquisition utilized a 15 kV accelerating voltage, 100 nA beam current and a fully focused beam. Pixel dimensions were chosen between as 0.5, 1, or 2 μm^2 depending on the size of the map area, and 150 ms per pixel dwell time. Data were processed using the Calcimage® software package and output to Surfer®.

Temperature maps were obtained by extracting each pixel from the WDS map as a XYZ point using Surfer® and exporting this as a.txt map. The.txt maps were then processed in Python by using the matplotlib package. For this an empty 3D stack was first created and then filled with the.txt maps for each element in the WDS maps. The 3D stack was then reshaped into a 2D array where each row contains the pixels of one element. The 2D array allowed us to work with pixels as elemental concentration data. First we isolated the actinolite grains from the rest of the map by using Ca combined with Si concentrations. Once we had all the pixels corresponding to the actinolite grains, we applied the Lledo and Jenkins (2008) polynomial regression on each pixel by using the Fe and Mg concentrations. Then we reshaped the resulting 2D data array back into a 3D one and plotted the temperature WDS map using the matplotlib function "imshow()". The final images obtained are those shown in Fig. 2a–e.

Data availability

The authors declare that the data supporting this study and needed to reproduce it are available within the paper, its supplementary information and stored at Science Data Bank https://doi.org/10.11922/sciencedb.01103.

Code availability

The authors declare that the code used for this research is publicly stored in Figshare https://doi.org/10.6084/m9.figshare.15125421.

Received: 8 December 2020; Accepted: 27 August 2021;
Published online: 15 September 2021

References

1. Groves, D. I., Bierlein, F. P., Meinert, L. D. & Hitzman, M. W. Iron oxide copper-gold (IOCG) deposits through earth histoiy: Implications for origin, lithospheric setting, and distinction from other epigenetic iron oxide deposits. *Econ. Geol.* **105**, 641–654 (2010).
2. Williams, P., Barton, M., Fontbote, L., Mark, G. & Marshick, R. Iron oxide copper-gold deposits: Geology, space-time distribution, and possible modes of origin. *Econ. Geol.* **100**, 371–405 (2005).
3. Barton, M. D. In *Treatise on Geochemistry: Second Edition*, vol. 13, 515–541 (Elsevier Ltd., 2013).
4. Apukhtina, O. B. et al. Early, deep magnetite-fluorapatite mineralization at the olympic dam Cu-U-Au-Ag deposit, South Australia. *Econ. Geol.* **112**, 1531–1542 (2017).
5. deMelo, G. H. C. et al. Temporal evolution of the giant Salobo IOCG deposit, Carajás Province (Brazil): constraints from paragenesis of hydrothermal alteration and U-Pb geochronology. *Miner. Depos.* **52**, 709–732 (2017).
6. del Real, I., Thompson, J. F. H. & Carriedo, J. Lithological and structural controls on the genesis of the Candelaria-Punta del Cobre Iron Oxide Copper Gold district, Northern Chile. *Ore Geol. Rev.* **102**, 106–153 (2018).
7. Sillitoe, R. Iron oxide-copper-gold deposits: an Andean view. *Miner. Depos.* **38**, 787–812 (2003).
8. Rusk, B. G. et al. Compositions of magnetite and sulfides from barren and mineralized IOCG deposits in the eastern succession of the Mt Isa Inlier, Australia BT—Geological Society of America (GSA), 2009 Portland GSA annual meeting. *Geol. Soc. Am.* **41**, 84 (2009).
9. Rusk, B. et al. *Hydrothermal Iron Oxide Copper-Gold & Related Deposits: a global perspective—advances in the understanding of IOCG deposits*, vol. 3, 201–218 (Australasian Institute of Mining and Metallurgy (AusIMM) Bulletin, 2010).

10. Monteiro, L. V. S. et al. Spatial and temporal zoning of hydrothermal alteration and mineralization in the Sossego iron oxide-copper-gold deposit, Carajás Mineral Province, Brazil: Paragenesis and stable isotope constraints. *Miner. Depos.* **43**, 129–159 (2008).
11. Montreuil, J.-F., Potter, E. G., Corriveau, L. & Davis, W. J. Element mobility patterns in magnetite-group IOCG systems: the Fab IOCG system, Northwest Territories, Canada. *Ore Geol. Rev.* **72**, 562–584 (2016).
12. Huang, X. W. et al. Trace element composition of iron oxides from IOCG and IOA deposits: relationship to hydrothermal alteration and deposit subtypes. *Miner. Depos.* **54**, 525–552 (2019).
13. Li, R. et al. Using integrated in-situ sulfide trace element geochemistry and sulfur isotopes to trace ore-forming fluids: example from the Mina Justa IOCG deposit (southern Perú). *Ore Geol. Rev.* **101**, 165–179 (2018).
14. Childress, T. M. et al. Formation of the Mantoverde iron oxide-copper-gold (IOCG) deposit, Chile: insights from Fe and O stable isotopes and comparisons with iron oxide-apatite (IOA) deposits. *Miner. Depos.* **55**, 1489–1504 (2020).
15. del Real, I., Thompson, J. F. H. F. H., Simon, A. C. & Reich, M. Geochemical and isotopic signature of pyrite as a proxy for fluid source and evolution in the Candelaria-Punta del Cobre Iron Oxide Copper-Gold District, Chile. *Econ. Geol.* **115**, 1493–1518 (2020).
16. Rodriguez-Mustafa, M. A. et al. A continuum from iron oxide copper-gold to iron oxide-apatite deposits: evidence from Fe and O stable isotopes and trace element chemistry of magnetite. *Econ. Geol.* **115**, 1443–1459 (2020).
17. Schlegel, T. U., Wagner, T., Boyce, A. & Heinrich, C. A. A magmatic source of hydrothermal sulfur for the Prominent Hill deposit and associated prospects in the Olympic iron oxide copper-gold (IOCG) province of South Australia. *Ore Geol. Rev.* **89**, 1058–1090 (2017).
18. Marschik, R. & Fontboté, L. The Candelaria-Punta del Cobre iron oxide Cu-Au (-Zn-Ag) deposits, Chile. *Econ. Geol.* **96**, 1799–1826 (2001).
19. Marschik, R. & Kendrick, M. A. Noble gas and halogen constraints on fluid sources in iron oxide-copper-gold mineralization: Mantoverde and La Candelaria, Northern Chile. *Miner. Depos.* **50**, 357–371 (2015).
20. Kendrick, M. A., Phillips, D. & Miller, J. M. L. Part I. Decrepitation and degassing behaviour of quartz up to 1560 °C: analysis of noble gases and halogens in complex fluid inclusion assemblages. *Geochim. Cosmochim. Acta* **70**, 2540–2561 (2006).
21. Schlegel, T. U., Wagner, T., Wälle, M. & Heinrich, C. A. Hematite breccia-hosted iron oxide copper-gold deposits require magmatic fluid components exposed to atmospheric oxidation: evidence from prominent hill, Gawler Craton, South Australia. *Econ. Geol.* **113**, 597–644 (2018).
22. Rieger, A. A., Marschik, R. & Diaz, M. The evolution of the hydrothermal IOCG system in the Mantoverde district, northern Chile: new evidence from microthermometry and stable isotope geochemistry. *Miner. Depos.* **47**, 359–369 (2012).
23. Lledo, H. L. & Jenkins, D. M. Experimental investigation of the upper thermal stability of Mg-rich actinolite; implications for Kiruna-type iron deposits. *J. Petrol.* **49**, 225–238 (2008).
24. Watson, E. B., Wark, A. D. A. & Thomas, A. J. B. Crystallization thermometers for zircon and rutile. *Contrib. Mineral Petrol.* **151**, 413–433 (2006).
25. Wilkinson, J. J. et al. The chlorite proximitor: a new tool for detecting porphyry ore deposits. *J. Geochem. Explor.* **152**, 10–26 (2015).
26. Wilkinson, J. J., Baker, M. J., Cooke, D. R. & Wilkinson, C. C. Exploration targeting in porphyry Cu systems using propylitic mineral chemistry: a case study of the El Teniente deposit, Chile. *Econ. Geol.* **115**, 771–791 (2020).
27. Cooke, D. R. et al. Using mineral chemistry to detect the location of concealed porphyry deposits—an example from Resolution, Arizona. in *International Applied Geochemistry Symposium*, 1–6 (Tucson, Arizona, 2014).
28. Jacobs, D. C. & Parry, W. T. Geochemistry of Biotite in the Santa Rita Porphyry Copper Deposit, New Mexico. *Econ. Geol.* **74**, 860–887 (1979).
29. Selby, D. & Nesbitt, B. E. Chemical composition of biotite form the casino porphyry Cu-Au-Mo mineralization, Yukon, Canada: Evaluation of magmatic and hydrothermal fluid chemistry. *Chem. Geol.* **171**, 77–93 (2000).
30. Afshooni, S. Z., Mirnejad, H., Esmaeily, D. & Asadi Haroni, H. A. Mineral chemistry of hydrothermal biotite from the Kahang porphyry copper deposit (NE Isfahan), Central Province of Iran. *Ore Geol. Rev.* **54**, 214–232 (2013).
31. Moshefi, P., Hosseinzadeh, M. R., Moayyed, M. & Lentz, D. R. Comparative study of mineral chemistry of four biotite types as geochemical indicators of mineralized and barren intrusions in the Sungun Porphyry Cu-Mo deposit, northwestern Iran. *Ore Geol. Rev.* **97**, 1–20 (2018).
32. Bilenker, L. D. et al. Fe–O stable isotope pairs elucidate a high-temperature origin of Chilean iron oxide-apatite deposits. *Geochim. Cosmochim. Acta* **177**, 94–104 (2016).
33. Hanley, J. J. & Bray, C. J. The trace metal content of amphibole as a pboximityindicatob fob Cu-Ni-PGE minebalization in the footwall of the sudbuby igneous complex, Ontabio, Canada. *Econ. Geol.* **104**, 113–125 (2009).
34. Rojas, P. A. et al. A genetic link between magnetite mineralization and diorite intrusion at the El Romeral iron oxide-apatite deposit, northern Chile. *Miner. Depos.* **53**, 947–966 (2018).
35. Craveiro, G. S., Villas, R. N. N. & Xavier, R. P. Mineral chemistry and geothermometry of alteration zones in the IOCG Cristalino deposit, Carajás Mineral Province, Brazil. *J. South Am. Earth Sci.* **92**, 481–505 (2019).
36. Marschik, R. et al. Age of Cu(-Fe_-Au mineralization and thermal evolution of the Punta del Cobre district, Chile. *Miner. Depos.* **32**, 531–546 (1997).
37. Palma, G., Barra, F., Reich, M., Simon, A. C. & Romero, R. A review of magnetite geochemistry of Chilean iron oxide-apatite (IOA) deposits and its implications for ore-forming processes. *Ore Geol. Rev.* **126**, 103748 (2020).
38. Marschik, R. & Söllner, F. Early cretaceous U-Pb zircon ages for the Copiapo plutonic complex and implications for the IOCG mineralization at Candelaria, Atacama Region, Chile. *Miner. Depos.* **41**, 785–801 (2006).
39. Green, C. J. et al. Metamorphic amphiboles in the Ironwood Iron-Formation, Gogebic Iron Range, Wisconsin: Implications for potential resource development. *Am. Mineral.* **105**, 1259–1269 (2020).
40. Ross, M., Nolan, R. P. & Nord, G. L. The search for asbestos within the Peter Mitchell Taconite iron ore mine, near Babbitt, Minnesota. *Regul. Toxicol. Pharmacol.* **52**, S43–S50 (2008).
41. Jenkins, D. M. & Bozhilov, K. N. Stability and thermodynamic properties of ferro-actinolite: a re-investigation. *Am. J. Sci.* **303**, 723–752 (2003).
42. Jamtveit, B. Oscillatory zonation patterns in hydrothermal grossular-andradite garnet: nonlinear dynamics in regions of immiscibility. *Am. Mineral.* **76**, 1319–1327 (1991).
43. Putnis, A., Fernandez-Diaz, L. & Prieto, M. Experimentally produced oscillatory zoning in the (Ba, Sr)SO4 solid solution. *Nature* **358**, 743–745 (1992).
44. Simon, A. C., Pettke, T., Candela, P. A., Piccoli, P. M. & Heinrich, C. A. Magnetite solubility and iron transport in magmatic-hydrothermal environments. *Geochim. Cosmochim. Acta* **68**, 4905–4914 (2004).
45. Scholten, L. et al. Solubility and speciation of iron in hydrothermal fluids. *Geochim. Cosmochim. Acta* **252**, 126–143 (2019).
46. Migdisov, A. A., Bychkov, A. Y., Williams-Jones, A. E. & van Hinsberg, V. J. A predictive model for the transport of copper by HCl-bearing water vapour in ore-forming magmatic-hydrothermal systems: Implications for copper porphyry ore formation. *Geochim. Cosmochim. Acta* **129**, 33–53 (2014).
47. Williams-Jones, A. & Migdisov, A. Experimental constraints on the transport and deposition of metals in ore-forming hydrothermal systems. *Soc. Econ. Geol. Spec. Publ.* **18**, 77–96 (2014).
48. Chen, H. et al. Contrasting fluids and reservoirs in the contiguous Marcona and Mina Justa iron oxide-Cu (-Ag-Au) deposits, south-central Perú. *Mineralium Deposita* **46**, 677–706 (2011).
49. Rojas, P. A. et al. New contributions to the understanding of Kiruna-type iron oxide-apatite deposits revealed by magnetite ore and gangue mineral geochemistry at the El Romeral deposit, Chile. *Ore Geol. Rev.* **93**, 413–435 (2018).
50. Chen, H. et al. Evolution of the Giant Marcona-Mina Justa Iron Oxide-Copper-Gold District, South-Central Peru. *Econ. Geol.* **105**, 155–185 (2010).
51. Salazar, E. et al. Trace element geochemistry of magnetite from the Cerro Negro Norte iron oxide−apatite deposit, northern Chile. *Miner. Depos.* **55**, 409–428 (2020).
52. Reich, M. et al. Trace element signature of pyrite from the los colorados iron oxide-apatite (IOA) Deposit, Chile: a missing link between andean ioa and iron oxide copper-gold systems? *Econ. Geol.* **111**, 743–761 (2016).
53. Benavides, J. et al. The Mantoverde iron oxide-copper-gold district, III Región, Chile: the role of regionally derived, nonmagmatic fluids in Chalcopyrite mineralization. *Econ. Geol.* **102**, 415–440 (2007).
54. De Haller, A. & Fontboté, L. The rauc-condestable iron oxide copper-gold deposit, central coast of peru: Ore and related hydrothermal alteration, sulfur isotopes, and thermodynamic constraints. *Econ. Geol.* **104**, 365–384 (2009).
55. Lopez, G. P., Hitzman, M. W. & Nelson, E. P. Alteration patterns and structural controls of the El Espino IOCG mining district, Chile. *Miner. Depos.* **49**, 235–259 (2014).
56. Knipping, J. L. et al. Trace elements in magnetite from massive iron oxide-apatite deposits indicate a combined formation by igneous and magmatic-hydrothermal processes. *Geochim. Cosmochim. Acta* **171**, 15–38 (2015).
57. Knipping, J. L. et al. Giant Kiruna-type deposits form by efficient flotation of magmatic magnetite suspensions. *Geology* **43**, 591–594 (2015).
58. Simon, A. C. et al. Kiruna-type iron oxide-apatite (IOA) and iron oxide copper-gold (IOCG) deposits form by a combination of igneous and magmatic-hydrothermal processes: evidence from the Chilean Iron Belt. *Soc. Econ. Geol. Special Publ.* **21**, 89–114 (2018).
59. Knipping, J. L., Webster, J. D., Simon, A. C. & Holtz, F. Accumulation of magnetite by flotation on bubbles during decompression of silicate magma. *Sci. Rep.* **9**, 1–7 (2019).
60. Troll, V. R. et al. Global Fe–O isotope correlation reveals magmatic origin of Kiruna-type apatite-iron-oxide ores. *Nat. Commun.* **10**, 1–12 (2019).

61. Oreskes, N. & Einaudi, M. T. Origin of rare earth element-enriched hematite breccias at the Olympic Dam Cu-U-Au-Ag deposit, Roxby Downs, South Australia. *Econ. Geol.* **85**, 1–28 (1990).
62. Espinoza, S., Véliz, H., Esquivel, J., Arias, J. & Moraga, A. The cupriferous province of the coastal range, northern Chile. *Andean Copper Depos.* **5**, 19–32 (1996).
63. Davidson, G. J., Paterson, H., Meffre, S. & Berry, R. F. Characteristics and origin of the oak dam East Breccia-Hosted, iron oxide Cu-U-(Au) Deposit: Olympic Dam region, Gawler Craton, South Australia. *Econ. Geol.* **102**, 1471–1498 (2007).
64. Barra, F. et al. Unraveling the origin of the Andean IOCG clan: a Re-Os isotope approach. *Ore Geol. Rev.* **81**, 62–78 (2017).
65. Ootes, L. et al. A Paleoproterozoic Andean-type iron oxide copper-gold environment, the Great Bear magmatic zone, Northwest Canada. *Ore Geol. Rev.* **81**, 123–139 (2017).
66. Corriveau, L., Montreuil, J. F. & Potter, E. G. Alteration facies linkages among iron oxide copper-gold, iron oxide-apatite, and affiliated deposits in the great bear magmatic zone, Northwest Territories, Canada. *Econ. Geol.* **111**, 2045–2072 (2016).
67. Chiaradia, M., Banks, D., Cliff, R., Marschik, R. & Haller, A. Origin of fluids in iron oxide-copper-gold deposits: constraints from δ37Cl, 87Sr/86Sri and Cl/Br. *Miner. Depos.* **41**, 565–573 (2006).
68. Scheuber, E. & Gonzalez, G. Tectonics of the Jurassic-Early Cretaceous magmatic arc of the north Chilean Coastal Cordillera (22°–26°S): a story of crustal deformation along a convergent plate boundary. *Tectonics* **18**, 895–910 (1999).
69. Pichowiak, S. In *Tectonics of the Southern Central Andes* 203–217 (Springer Berlin Heidelberg, 1994).
70. Wallace, P. J. Volatiles in subduction zone magmas: concentrations and fluxes based on melt inclusion and volcanic gas data. *J. Volcanol. Geotherm. Res.* **140**, 217–240 (2005).
71. De Vivo, B., Lima, A. & Webster, J. D. Volatiles in magmatic-volcanic systems. *Elements* **1**, 19–24 (2005).
72. Hurwitz, S. & Navon, O. Bubble nucleation in rhyolitic melts: experiments at high pressure, temperature, and water content. *Earth Planet. Sci. Lett.* **122**, 267–280 (1994).
73. Pleše, P. et al. Dynamic observations of vesiculation reveal the role of silicate crystals in bubble nucleation and growth in andesitic magmas. *Lithos* **296–299**, 532–546 (2018).
74. Blundy, J., Mavrogenes, J., Tattitch, B., Sparks, S. & Gilmer, A. Generation of porphyry copper deposits by gas-brine reaction in volcanic arcs. *Nat. Geosci.* **8**, 235–240 (2015).
75. Rivalta, E. & Dahm, T. Acceleration of buoyancy-driven fractures and magmatic dikes beneath the free surface. *Geophys. J. Int.* **166**, 1424–1439 (2006).
76. Chelle-Michou, C., Rottier, B., Caricchi, L. & Simpson, G. Tempo of magma degassing and the genesis of porphyry copper deposits. *Sci. Rep.* **7**, 1–12 (2017).
77. Parmigiani, A., Degruyter, W., Leclaire, S., Huber, C. & Bachmann, O. The mechanics of shallow magma reservoir outgassing. *Geochem. Geophys. Geosyst.* **18**, 2887–2905 (2017).
78. Candela, P. A. Combined chemical and physical model for plutonic devolatilization: a non-Rayleigh fractionation algorithm. *Geochim. Cosmochim. Acta* **58**, 2157–2167 (1994).
79. Cox, S. F. Coupling between deformation, fluid pressures, and fluid flow in Ore-producing hydrothermal systems at depth in the crust. *Econ. Geol.* **100**, 39–75 (2005).
80. Cox, S. F. Injection-driven swarm seismicity and permeability enhancement: Implications for the dynamics of hydrothermal ore systems in high fluid-flux, overpressured faulting regimes—an invited paper. *Econ. Geol.* **111**, 559–587 (2016).
81. Sibson, R. H. Selective fault reactivation during basin inversion: potential for fluid redistribution through fault-valve action. *Geol. Soc. Lond. Spec. Publ.* **88**, 3–19 (1995).
82. Sibson, R. H., Robert, F. & Poulsen, K. H. High-angle reverse faults, fluid-pressure cycling, and mesothermal gold-quartz deposits. *Geology* **16**, 551 (1988).
83. Haynes, D. W., Cross, K. C., Bills, R. T. & Reed, M. H. Olympic Dam ore genesis: a fluid mixing model. *Econ. Geol.* **90**, 281–307 (1995).
84. Roberts, D. E. & Hudson, G. R. T. The Olympic Dam copper-uranium-gold deposit, Roxby Downs, South Australia. *Econ. Geol.* **78**, 799–822 (1983).
85. Zhao, J., Brugger, J., Chen, G., Ngothai, Y. & Pring, A. Experimental study of the formation of chalcopyrite and bornite via the sulfidation of hematite: Mineral replacements with a large volume increase. *Am. Mineral.* **99**, 343–354 (2014).
86. Audétat, A., Simon, A., Hedenquist, J., Harris, M. & Camus, F. In *Geology and genesis of major copper deposits and districts of the world-A tribute to Richard H. Sillitoe* 553–572 (Society of Economic Geologists, 2012).
87. Audétat, A. The metal content of magmatic-hydrothermal fluids and its relationship to mineralization potential. *Econ. Geol.* **114**, 1033–1056 (2019).
88. Halter, W. E., Pettke, T. & Heinrich, C. A. The origin of Cu/Au ratios in porphyry-type ore deposits. *Science* **296**, 1844–1846 (2002).
89. Veloso, E. A. et al. Trace elements distribution in magnetite: the relationship between tectonics and hydrothermal fluid flow in the Dominga Fe-Cu deposit, Coastal Cordillera, Northern Chile. *American Geophysical Union, Fall Meeting (AGUFM)* **2019**, V33C–0259 (2019).

Acknowledgements

This study was funded by ANID through Millennium Science Initiative Program (NCN13_065) to M.R. and Fondecyt postdoctoral Grant 3200532 to I.D.R. Additional support was provided by ANID through FONDECYT grant #1190105. A.C.S. acknowledges support from NSF EAR #1924142. All samples were obtained from the Candelaria deposit with permission from Lundin Mining. Lundin Mining is acknowledged for their field support.

Author contributions

All the authors contributed substantially to the paper as a team including sampling, data acquisition and interpretation, construction of the model, and writing. I.D.R. and M.R. conceived and designed the study. EPMA data acquisition was carried out by I.D.R., A.D., and M.P.R. Actinolite thermometry and compositional data inversion in WDS maps was carried out by I.D.R. under the supervision of M.R. The conception of the evolution model was proposed by I.D.R. and M.R. with substantial contribution and discussion with F.B., A.S., J.T., A.D., and M.R. All the authors analyzed and discussed the data and revised the manuscript, which was written by I.D.R. and M.R.

Competing interests

The authors declare no competing interests.

Additional information

Supplementary information The online version contains supplementary material available at https://doi.org/10.1038/s43247-021-00265-w.

Correspondence and requests for materials should be addressed to Irene Del Real..

Peer review information *Communications Earth & Environment* thanks the anonymous reviewers for their contribution to the peer review of this work. Primary Handling Editor: Joe Aslin. Peer reviewer reports are available.

Reprints and permission information is available at http://www.nature.com/reprints

Publisher's note Springer Nature remains neutral with regard to jurisdictional claims in published maps and institutional affiliations.